



On the structural and electrical properties of MgFe_2O_4 , $\text{MgMn}_{0.2}\text{Fe}_{1.8}\text{O}_4$, and Mn_3O_4

F. Farshidfar, M. Lapolla, A. Fattahi, K. Ghandi*

Department of Chemistry, University of Guelph, Guelph, ON, N1G 2W1, Canada

ARTICLE INFO

Keywords:

Ceramics
Disordered systems
Inorganic materials
Anisotropy
Electrical transport

ABSTRACT

Charge carrier transport via donor/acceptor pairs of similar elements is dominant in n-type MgFe_2O_4 and p-type Mn_3O_4 spinels. The temperature-independent activation energy in the form of the nearest neighbor hopping model is applied for $\text{Fe}^{2+}/\text{Fe}^{3+}$ pairs of cubic MgFe_2O_4 spinel in the temperature range of 423–523 K (150–250 °C). At such high temperatures, even for this relatively narrow temperature range, the constant energy barrier deviates to a variable range hopping energy barrier in the case of Mn_3O_4 , due to Jahn-Teller active octahedral sites. Replacing 10 mol% of Fe at octahedral sites with Mn has significantly increased the electron hopping energy barrier and electrical conductivity of MgFe_2O_4 , while keeping the nearest neighbor hopping model dominant. The observed high energy barrier is due to donor/acceptor pairs of different elements (Mn/Fe). Due to a lack of structural distortion, deviation from the nearest neighbor hopping mechanism with temperature-independent activation energy was not observed. Rietveld refined XRD patterns and FT-IR spectra are utilized to support the argument on electrical conductivity mechanisms.

1. Introduction

Metal oxides classified as spinels are widely applied as sensors [1,2], catalysts [3], photocatalysts [4], and electrocatalysts [5], wherein the electrical properties play a crucial role. In particular, appropriate structural changes to spinels can improve the electron transport on the surface [6], which increases the electrical conductivity and hence the catalytic activity on the surface. Spinel is a group of AB_2O_4 metal oxides, also referred to as 2–3 spinels, where A and B are divalent and trivalent cations, respectively [7]. The unit cell of spinels contains 32 octahedral sites and 64 tetrahedral sites. Usually, the divalent A cations are in 8 tetrahedral sites and B cations in 16 octahedral sites [7,8]. The distribution of cations among tetrahedral and octahedral sites is described by inversion degree. To demonstrate the cation distribution of AB_2O_4 , a general formula of $(\text{A}_{1-\alpha}\text{B}_\alpha)[\text{A}_\alpha\text{B}_{2-\alpha}]\text{O}_4$ is regularly utilized where parentheses represent tetrahedral sites and square brackets represent octahedral sites. α is referred to as the inversion degree, describing the distribution of cations contained by each site [9,10]. The spinel is either normal or inverted for the cases where α is 0 and 1, respectively. However, any value of α between 0 and 1 indicates a random distribution of cations within the spinel denoted as mixed, or partially inverted. MgFe_2O_4 and Mn_3O_4 are spinels configured in the form of inverted and normal respectively based on octahedral preference of cations. Hence, they are demonstrated in the forms of $(\text{Fe}^{3+})[\text{Mg}^{2+}, \text{Fe}^{3+}]\text{O}_4$ and $(\text{Mn}^{2+})[\text{Mn}^{3+}]\text{O}_4$ in terms of cation distribution [11–13].

* Corresponding author.

E-mail address: kghandi@uoguelph.ca (K. Ghandi).

<https://doi.org/10.1016/j.heliyon.2023.e21677>

Received 7 May 2023; Received in revised form 21 October 2023; Accepted 25 October 2023

Available online 28 October 2023

2405-8440/© 2023 Published by Elsevier Ltd.

This is an open access article under the CC BY-NC-ND license

(<http://creativecommons.org/licenses/by-nc-nd/4.0/>).

Bulk octahedral sites share their edges with 6 neighboring octahedral sites [8,14]. If two octahedral neighbors are occupied by a cation with d-orbital outer shell, such as Fe^{3+} , a double exchange interaction of $[\text{Fe}]\text{-O-}[\text{Fe}]$ couples their spin orientations in parallel [15]. Octahedral sites share their corners with tetrahedral sites, leading to a superexchange interaction of $[\text{Fe}]\text{-O-}(\text{Fe})$, and couples the spin orientations of two adjacent iron cations antiparallel [15,16]. Unlike parallel coupling, based on the simplified treatment of localized spins for strong exchange interaction, the antiparallel spin arrangement prohibits electron transport between tetrahedral and octahedral sites. Electrons cannot move easily if the spin angles between two adjacent sites is equal to π as in antiferromagnetic ordering [17]. Hence, double exchange interaction between octahedral sites plays dominant role in electrical properties [18].

MgFe_2O_4 is an inverted ferrite spinel with n-type semiconductor behavior in which electrons hop through the structure as the main charge carrier [19,20]. Electron hopping occurs via double exchange interactions between octahedral sites, converting $[\text{Fe}^{2+}]\text{-O-}[\text{Fe}^{3+}]$ to $[\text{Fe}^{3+}]\text{-O-}[\text{Fe}^{2+}]$ [21]. Mn_3O_4 is a Mn-based normal spinel where most tetrahedral sites are occupied by Mn^{2+} . Octahedral sites are mainly occupied by Mn^{3+} and partially by Mn^{4+} [13]. Charge transport in the form of electron holes demonstrates a p-type behavior occurring through the double exchange interaction, expectedly converting $[\text{Mn}^{4+}]\text{-O-}[\text{Mn}^{3+}]$ to $[\text{Mn}^{3+}]\text{-O-}[\text{Mn}^{4+}]$. Charge transport through MgFe_2O_4 and Mn_3O_4 are dominated by $\text{Fe}^{2+}/\text{Fe}^{3+}$ and $\text{Mn}^{4+}/\text{Mn}^{3+}$ donor/acceptor pairs, respectively.

Our previous work explored the development of a heterogenous heterojunction comprised of Mn_3O_4 and MgFe_2O_4 , where the tunability of these composites affected various physicochemical properties within the material [22]. Here, we intend to build upon our previous work by implementing a homogenous semiconductor instead and probe the electron transport and hopping mechanisms of this material compared to the non-composite pure spinels, Mn_3O_4 and MgFe_2O_4 . This paper aims to investigate electron transport on the surfaces of spinels, focusing specifically on cubic MgFe_2O_4 and non-cubic Mn_3O_4 . Through this, we may determine whether structural deviations impact the electron hopping mechanism. In addition, this study is exploring cubic ferrite spinel where 10 mol% of Fe was replaced with Mn, considering the fact that Mn^{3+}O_6 is a Jahn-Teller active octahedral [23,24]. 10 mol% Fe was chosen to maintain a cubic structure within the material. Our unpublished data shows that including amounts above this would cause significant deviation from a cubic structure. Lastly, we are also exploring a relatively high temperature for variable range hopping in a non-cubic spinel, which is another unique aspect to our study.

2. Materials and methods

All analytical grades of starting materials were used as received. The standard co-precipitation method was utilized to form MgFe_2O_4 spinel using $\text{Mg}(\text{NO}_3)_2 \cdot 6\text{H}_2\text{O}$ (Sigma-Aldrich, ACS reagent 99 %), $\text{Fe}(\text{NO}_3)_3 \cdot 9\text{H}_2\text{O}$ (Sigma-Aldrich, ACS reagent, >98 %), and NaOH (Sigma-Aldrich, >98 %) as precipitation agent similar to our previous report [6]. To prepare Mn doped MgFe_2O_4 , Mn_3O_4 powder (Sigma-Aldrich, 10 μm , >97 %) was dry mixed thoroughly with finely powdered as prepared precipitate of MgFe_2O_4 with appropriate composition. Powders were compressed into pellets using a hydraulic press, resulting in a pellet diameter of 15 mm and thickness of 2 mm. This was followed by heating under an air atmosphere at 1300 $^\circ\text{C}$ for 3 h to form the spinel structure. Pure Mn_3O_4 was prepared using Mn_3O_4 powder (Sigma-Aldrich, 10 μm , >97 %) as a starting material.

Square shaped samples (10 mm \times 6 mm \times 1 mm) were prepared by polishing all sides and edges followed by applying two silver

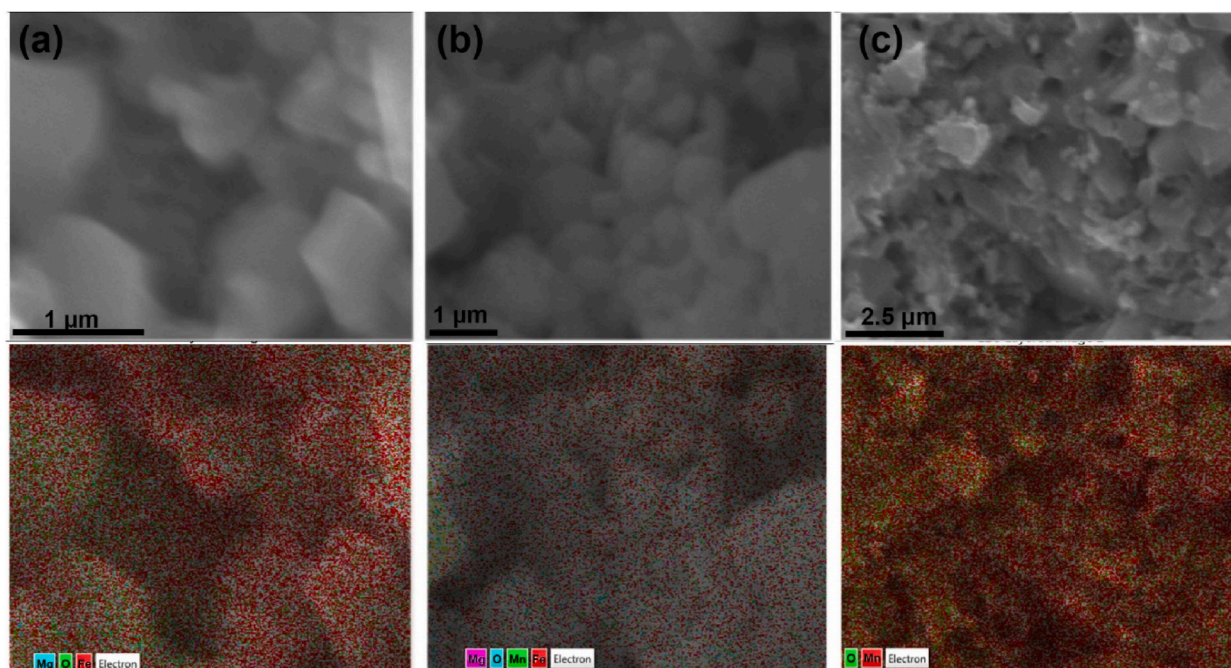


Fig. 1. SEM images of (a): MgFe_2O_4 , (b): $\text{MgMn}_{0.2}\text{Fe}_{1.8}\text{O}_4$, and (c): Mn_3O_4 and corresponding EDX map.

electrodes (2 mm × 6 mm) on one polished side using highly conductive silver paste (Sigma-Aldrich, 200 nm 80 %). A simple two contact measuring method of electrical resistance was carried out in both directions through switching the prods of a voltmeter (Fluke, Model 117 RMS). The average of two values was recorded at any preferred temperature. PXRD measurements were performed using a PANalytical Empyrean diffractometer in a reflection (Bragg–Brentano) geometry with Cu K α radiation source, Ni K β filter, and PIXcel1D linear detector. A powdered sample was loaded into a sample holder with a 16 mm insert, which was mounted on a spinning stage at room temperature. Powder diffractograms were recorded in the 5–110° 2 θ range with a step size of 0.0131° and exposure time of 60 s per step. Data collection was controlled with the Data Collector software [25]. A smoothing function was applied using HighScore Plus (version 4.1) [26]. The Rietveld refinement of XRD patterns were carried out accurately in both visual and statistical aspects using Materials Analysis Using Diffraction (MAUD) version 2.992. Values of R_p denoted as profile parameter and R_{wp} as weighted profile parameter were determined to confirm the accuracy of refinement [27]. Calculations of the crystal size and crystal strain were performed according to the Williamson-Hall method. FTIR spectra was collected by compact Bruker (ALPHA II) instrument in the wavenumber range of 380 cm⁻¹–4000 cm⁻¹.

Differential scanning calorimetry (DSC) measurements were done to determine if any phase change would occur due to heating during the electrical conductivity measurements. This was carried out with a Mettler Toledo DSC 3 instrument, with analysis performed by the equipment software (STARe). Approximately 8–16 mg of the samples were crushed with a mortar and pestle. They were then loaded into 100 μ L aluminum crucibles with pierced lids. A rate of 20 °C/min was used during heating and for cooling back down to room temperature, for a total of 4 cycles. The furnace was kept under a reactive atmosphere using Ultra Zero compressed air (~5 PSI, 200 mL/min) to mimic the conditions of the electrical conductivity measurements. The cooling phase of the final cycle is considered to confirm the phase transitions (or lack thereof). The morphologies of the products were characterized by scanning electron microscopy (SEM, FEI inspect S50) capable of performing energy dispersive X-ray spectroscopy (EDS).

3. Results and discussion

SEM images and corresponding EDXs are shown in Fig. 1 (a to c). Fig. 1(b) confirms the homogenous distribution of Mn throughout MgMn_{0.2}Fe_{1.8}O₄. In addition, MgFe₂O₄ was Mn free, and Mn₃O₄ was Fe and Mg free as shown in Fig. 1(a) and (c) respectively. Particle size is in the range of sub-micron for all three samples.

The electrical properties are discussed in terms of DC-electrical conductivity measured at the temperature range where there was no phase transition which is from 150 °C - 250 °C, established by our DSC measurements. DSC confirmed no phase transition within this temperature range as shown in Fig. 2.

Rietveld refined XRD pattern of MgFe₂O₄, MgMn_{0.2}Fe_{1.8}O₄, and Mn₃O₄ are shown in Fig. 3 (a); XRD pattern of MgFe₂O₄, MgMn_{0.2}Fe_{1.8}O₄, and Mn₃O₄ spinels treated at 1300 °C with corresponding difference between experimental and fitted model, (b): comparison of (311) peaks designated by * for Mn-doped (or MgMn_{0.2}Fe_{1.8}O₄) and undoped MgFe₂O₄ (c): Crystallite size and strain of each sample extracted from the XRD refinement based on the method we described in the section on materials and methods.

Crystallization of Mn₃O₄ fits in the I4₁/amd space group of tetragonal crystal structure based on the Jahn-Teller effect of Mn³⁺ at octahedral site. Both MgFe₂O₄ and MgMn_{0.2}Fe_{1.8}O₄ fit in fd3m space group of a cubic crystal structure. This confirms that replacing 10 mol% of Fe with Mn cation will not cause significant deviation from the typical cubic structure. However, Fig. 3 (b) displays a shift of the (311) peak towards a lower degree, which agrees with increasing interplanar distance. Increasing structural strain, ϵ , as illustrated in Fig. 3 (c), supports the structural tensions generated within MgFe₂O₄ by Mn diffusion. Crystallite size is 200 nm and 133 nm in Mn₃O₄ and MgFe₂O₄, respectively. This is also consistent with our SEM observations in Fig. 1, although the SEM cannot provide an accurate size for these samples. It is also worth noting that Mn diffusion has affected neither the crystallite size nor crystal structure of

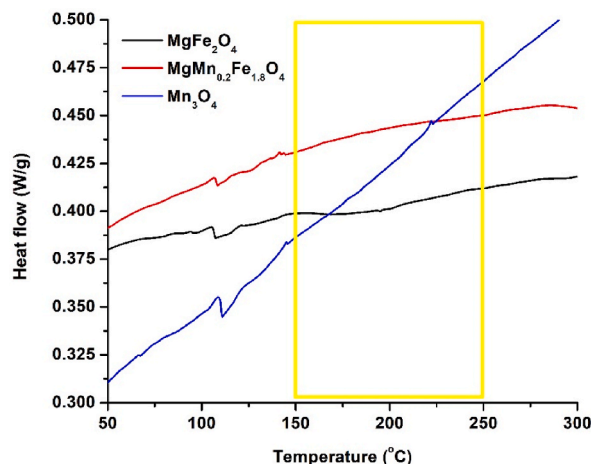


Fig. 2. DSC of the samples: electrical conductivity measurement is carried out at the highlighted temperature range where there is no phase transition detected.

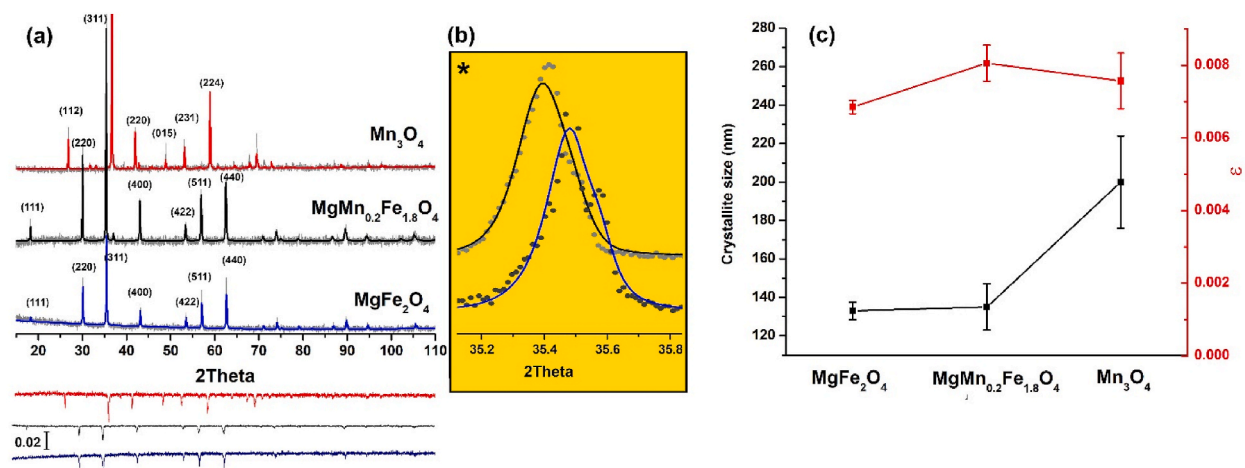


Fig. 3. (a): XRD pattern of MgFe₂O₄, MgMn_{0.2}Fe_{1.8}O₄, and Mn₃O₄ spinels treated at 1300 °C with corresponding difference between experimental and fitted model, (b): comparison of (311) peaks designated by * for Mn-doped (or MgMn_{0.2}Fe_{1.8}O₄) and undoped MgFe₂O₄ (c): Crystallite size and strain of each sample extracted from the XRD refinement.

MgFe₂O₄ significantly, hence enabling us to discuss electron transport through Mn incorporated cubic ferrite.

Rietveld refinement process of XRD patterns is done with R_{wp} below 10 % and goodness of fit a little bit larger than one [28]. The extracted structural parameters are summarized in Table 1. Increasing the Lattice parameter of MgFe₂O₄ structure from 8.381(1) Å to 8.401(1) Å by Mn doping shows a structural expansion, which is partially due to increased interlayer spacing, increasing the distance between octahedral sites. It should be noted that the distance between octahedral sites at pure Mn₃O₄ is in the range of 3.001 Å and 3.252 Å, both of which values are larger than undoped and Mn-doped MgFe₂O₄. Hence, the electron hopping distance in Mn doped MgFe₂O₄ spinel is shorter than electron hopping distance in the Mn₃O₄ spinel.

The structural effect of Jahn-Teller active Mn³⁺O₆ is illustrated in Fig. 4(a), showing elongation in the z direction to fit in an octahedral crystal site. Referring to crystal field theory, one electron occupancy of e_g removes its orbital degeneracy, leading to the elongation of 2x Mn³⁺-O bonds to 2.374(1) Å. The 4x Mn³⁺-O bonds are shortened as represented by “2” and “1” in Fig. 4(b), respectively. Octahedral sites of Mn₃O₄ are occupied mainly by Mn³⁺ due to normal cation distribution, generating significant anisotropic dimensions. The distortion index Δ_d of MnO₆ octahedral equals 0.62 which is higher than the limit of 10⁻³, indicating the significant distortion of the MnO₆ site [29]. As a result of such structural distortion, there will be a range of [oct.]-[oct.] distance between 3.001 Å and 3.252 Å. The distance between Mn cations occupying two octahedral sites is at a minimum where octahedral sites share edges of shortened oxygen bonds. The distance of Mn cations will increase by sharing edges that contain an elongated oxygen bond. Mn³⁺ cations with less distance are distributed in XY-plane, and Mn³⁺ cations with a larger distance from each other are distributed in XZ and YZ-planes.

The ratio of XRD peak intensities of (400) and (422) is utilized to extract the iron distribution based on the Bertaut method [30],

Table 1

Rietveld refined structural parameters.

parameter	unit	Mn ₃ O ₄	MgMn _{0.2} Fe _{1.8} O ₄	MgFe ₂ O ₄
R_{wp}	%	6.91	3.78	4.93
R_p		4.7	2.8	3.9
R_{exp}		4.46	3.06	4.27
Goodness of fit	χ^2	1.55	1.23	1.15
a	Å	5.873(1)	8.401(1)	8.381(1)
b		5.870(1)		
c		9.600(1)		
V		330.95	592.91	588.69
[Oct.]-O		2.374,1.907,2.004	2.196	2.122
[Oct.]-[Oct.]		3.001–3.252	2.970	2.963
Theoretical density	g/cm ³	4.59	4.48	4.51
Observed density		3.14	3.87	3.77
Porosity*	%	31.6	13.6	16.4
Crystallite size	nm	133 ± 4.5	135 ± 12	200 ± 24
I(400)/I(422)			2.5	1.8
Cation distribution		(Mn ²⁺)[Mn ³⁺] ₂ O ₄	(Fe ³⁺ _{0.64} Mg ²⁺ _{0.36})[Mg ²⁺ _{0.64} Mn ³⁺ _{0.20} Fe ³⁺ _{1.16}]O ₄	(Fe ³⁺ _{0.80} Mg ²⁺ _{0.20})[Mg ²⁺ _{0.80} Fe ³⁺ _{1.20}]O ₄

R_p : Profile parameter (not weighted).

R_{wp} : Weighted profile parameter.

*%Porosity = (1-observed density/theoretical density) x100.

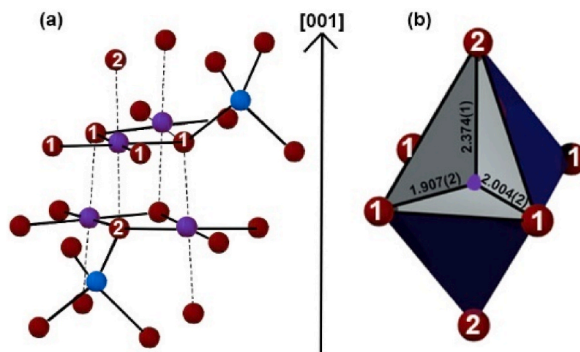


Fig. 4. (a): Structural effect of Jahn-Teller active $Mn^{3+}O_6$ octahedral in Mn_3O_4 spinel. Red, purple, and light-blue atoms are oxygen, Mn^{3+} , and Mn^{2+} atoms, respectively. Dashed lines are elongated $Mn^{3+}-O$ bonds; (b): $Mn^{3+}O_6$ octahedra with elongated bond in z direction; 4x shortened oxygens bonds are represented by 1, and 2x elongated oxygen bonds are represented by 2.

according to equation (1).

$$\frac{I_{(400)}}{I_{(422)}} = \frac{(8(-F_{(A)} + 2F_{(B)} + 4F_{(O)}))^2 P_{400} L_{400}}{(8F_{(A)})^2 P_{422} L_{422}} \tag{1}$$

where F , P , and L are structure, multiplicity, and Lorentz polarization factors, respectively. For $MgFe_2O_4$, the $I_{(400)}/I_{(422)}$ ratio is 1.8, corresponding to an inversion degree of 0.80, while for $MgMn_{0.2}Fe_{1.8}O_4$, the $I_{(400)}/I_{(422)}$ ratio is 2.5, corresponding to an inversion degree of 0.64. Mn doping in $MgFe_2O_4$ reduces the inversion degree by moving Mg cations from octahedral sites to tetrahedral sites, due to higher octahedral site stabilization energy of Mn^{3+} [31]. Hence, octahedral sites of $MgMn_{0.2}Fe_{1.8}O_4$ are more enriched with transition metals of Mn and Fe compared with $MgFe_2O_4$.

Two models including thermal excitation electron hopping (TEH) and three-dimensional variable range hopping (3d-VRH) are applied which are based on temperature independent and temperature dependent activation energies respectively [19,32]. Electrical conductivity models follow equations (2) and (3):

$$\text{Thermal excitation hopping (TEH)} \sigma = \sigma_0 \exp\left(-\frac{E_a}{k_B T}\right) \tag{2}$$

$$\text{Three - dimensional variable range hopping (3d - VRH)} \sigma = \frac{\sigma_0}{T^{\frac{1}{4}}} \exp\left(-\left(\frac{T_0}{T}\right)^{\frac{1}{4}}\right) \tag{3}$$

where σ is the electrical conductivity, σ_0 is the pre-exponential factor, k_B is the Boltzmann constant in eV/K, and T is temperature in K, T_0 is the characteristic temperature corresponding to activation energy.

If the electrical conductivity fits Eq. (2) the nearest neighbor hopping (NNH) model for electrons is the preferred model with

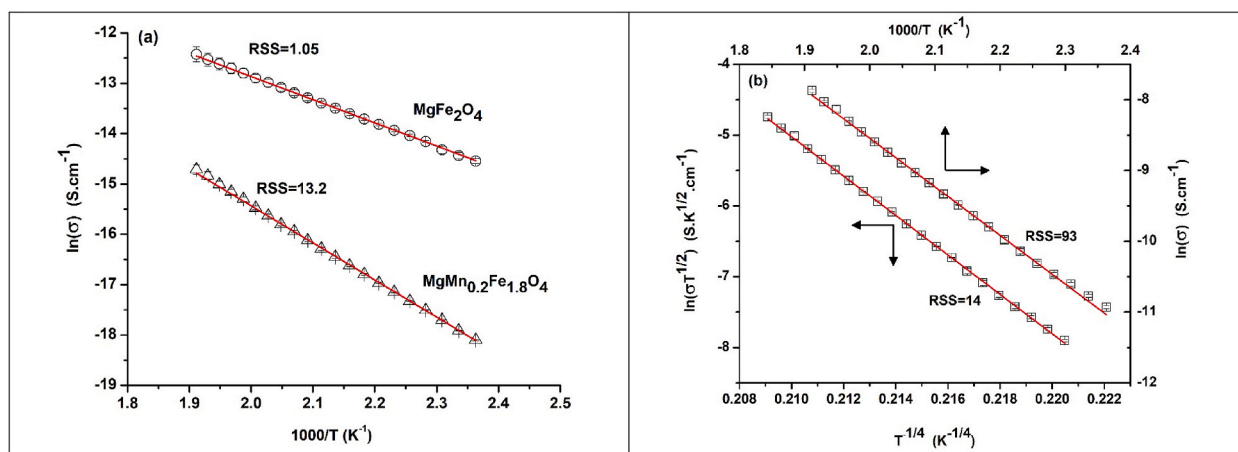


Fig. 5. Conductivity as a function of temperature according to (a): applied thermal excitation hopping (TEH) model on $MgFe_2O_4$ and $MgMn_{0.2}Fe_{1.8}O_4$ and corresponding weighted residual sum of square (RSS) of linear fittings, (b): 3d-variable range hopping (3d-VRH) model and corresponding weighted residual sum of square (RSS) of linear fittings for Mn_3O_4 .

temperature independent activation energy [33,34]. The energy barriers of thermal electron hopping are extracted by investigating $\ln(\sigma)$ and $\ln(\sigma T)$ vs $1000/T$, shown in Fig. 5. In variable range electron hopping models, the energetically preferred hopping sites are considered to be beyond the nearest neighbor, hence, the energy barrier becomes temperature dependent [19]. The energy barrier of the variable range electron hopping model corresponds to the characteristic temperature shown as T_0 , which is the slope of the $\ln(\sigma T)$ vs $T^{1/p}$, where $p = 4$ for three-dimensional variable range electron hopping.

The weighted Residual Sum of Square (RSS) of fits for these models to the experimental data were used to determine the mechanism of electron hopping outlined in Fig. 5(a and b). Thermal hopping model fits $MgFe_2O_4$ spinel data well with the RSS value of 1.05, indicating that the TEH model is represented accurately by the trends in the data. The RSS value increases for $MgMn_{0.2}Fe_{1.8}O_4$ data to 13.2, but still fits well as obvious in Fig. 5(a). $MgMn_{0.2}Fe_{1.8}O_4$ being crystallized in a cubic structure causes internal lattice strain, increasing the RSS value of the nearest neighbor hopping model. The RSS value significantly increases if Mn_3O_4 data is fitted to the NNH model. However, when the 3d-VRH model is applied to the Mn_3O_4 data, the RSS value drastically decreases from 93 to 14 (Fig. 5 (b)).

The electrical conductivity at the temperature range of 150–250 °C is in the order of $Mn_3O_4 > MgFe_2O_4 > MgMn_{0.2}Fe_{1.8}O_4$. High electrical conductivity can be attributed to a greater occupancy of octahedral sites by transition metal cations. In Mn_3O_4 , a normal spinel configuration prevails, where all Mn^{3+} cations reside within octahedral sites, actively participating in electron transport. In contrast, $MgFe_2O_4$ is an inverse spinel, where half of Fe^{3+} are replaced by Mg^{2+} , which has a poor contribution in electron transport. More interestingly, $MgFe_2O_4$ becomes electrically less conductive by Mn doping, as discussed later.

The average energy barrier extracted from the thermal electron hopping model shown in Fig. 6 is in the order of $MgMn_{0.2}Fe_{1.8}O_4 > Mn_3O_4 > MgFe_2O_4$. The energy barrier of $MgFe_2O_4$ and Mn_3O_4 are in good agreement with previous reports [35–38]. Considering the VRH model to describe the electron transport through Mn_3O_4 , the hopping energy barrier would change with the temperature according to equation (4),

$$E_a(T) = \frac{1}{4}k_B T^{\frac{3}{4}} T_0^{\frac{1}{4}} \tag{4}$$

where T_0 is the characteristic temperature. The hopping energy through Mn_3O_4 in the temperature range of 420–520 K is in the range of 0.56–0.66 eV as shown in Fig. 6, increasing with temperature. Variable range electron hopping at such a high temperature has not been reported for Jahn-teller active Mn_3O_4 before this work, but is observed in similar non-cubic structures such as Pr_2ZnMnO_6 and Pr_2NiTiO_6 at the temperature range of 300–580 K [29] and 164–490 K [39,40], respectively. The electron hopping activation energy is higher at Mn_3O_4 compared to $MgFe_2O_4$ due to an increased hopping distance originating from the Jahn-Teller effect. $MgMn_{0.2}Fe_{1.8}O_4$ spinel shows the poorest electrical conductivity with the highest electron hopping activation energy amongst all samples.

Pre-exponential factor (σ_0) provides information about the probability of electron hopping between octahedral sites, and it is expressed by equation (5).

$$\sigma_0 = \frac{gNc(1-c)e^2a^2\vartheta}{k_B} \tag{5}$$

where N is the total density of charge carriers at octahedral sites, g is the geometric factor, a is the hopping distance, e is the electron charge, ϑ is the acoustic phonon frequency in Hz, and $c(1-c)$ is the hopping probability [41]. Regarding $MgFe_2O_4$, the hopping

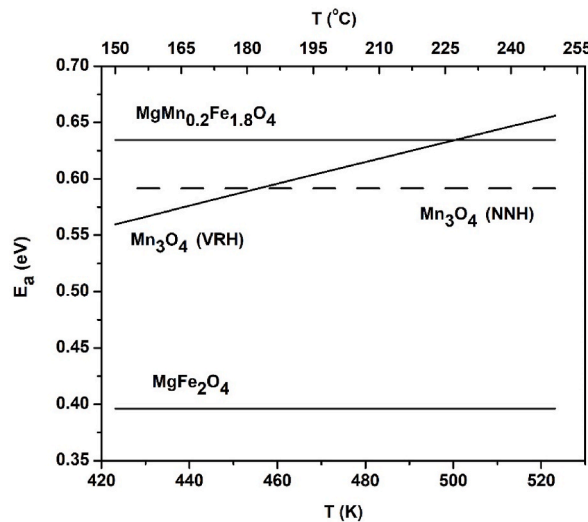


Fig. 6. Activation energy of electron hopping in $MgFe_2O_4$, $MgMn_{0.2}Fe_{1.8}O_4$, Mn_3O_4 based on nearest neighbor hopping (NNH) model and Variable range hopping (VRH) model.

probability (c) corresponds to the number of nearest neighbors in Fe^{3+}O_6 coordination, out of the 6 edge-sharing octahedral sites surrounding Fe^{2+}O_6 . For Mn_3O_4 , the hopping probability corresponds to the number of Mn^{3+}O_6 sites out of the 6 edge-sharing octahedral sites surrounding Mn^{4+}O_6 . A similar hopping probability is observed for MgFe_2O_4 and $\text{MgMn}_{0.2}\text{Fe}_{1.8}\text{O}_4$, which have similar structural dimensions with similar hopping distances. However, both MgFe_2O_4 and $\text{MgMn}_{0.2}\text{Fe}_{1.8}\text{O}_4$ exhibit a lower pre-exponential factor than Mn_3O_4 because of fewer donor/acceptor pairs due to Mg cations occupying octahedral sites. Mg has a relatively poor contribution in electron transport, negatively impacting the available sites of electron hopping. Longer hopping length (α) in Mn_3O_4 is also effective for increasing the preexponential factor.

FT-IR spectra is impacted by the cation-anion interaction at the octahedral sites which has significant role in electron hopping mechanism. The FT-IR analysis of Mn_3O_4 revealed three peaks in the range of 400–600 cm^{-1} , because of Jahn-Teller induced structural distortion. Mn–O vibrations at tetrahedral sites appear at 655 cm^{-1} and Mn–O vibrations at octahedral sites appear at 405 cm^{-1} and 564 cm^{-1} [21,42]. In the context of the MgFe_2O_4 spinel structure, vibrational modes linked to both the tetrahedral and octahedral sites manifest as two discernible peaks in the range of 400–650 cm^{-1} . This also confirms the formation of spinel. Notably, a distinct peak at 445 cm^{-1} can be ascribed to the octahedral site, whereas the peak at 615 cm^{-1} corresponds to the tetrahedral site [43]. As a result of structural expansion of these sites, a red shift occurs towards lower wavenumbers, arising from an accumulation of Mn cations in the doped MgFe_2O_4 . In addition to the observed shift, both peaks are wider in $\text{MgMn}_{0.2}\text{Fe}_{1.8}\text{O}_4$, due to the presence of both Fe and Mn cations at tetrahedral and octahedral sites. FT-IR spectra of undoped and doped samples are illustrated in Fig. 7.

Since electron hopping occurs via oxygen sharing at octahedral sites, enlargement of octahedral sites negatively impacts the hopping activation energy by reducing the cation-anion orbital overlap. Hence, the higher electron hopping activation energy of cubic $\text{MgMn}_{0.2}\text{Fe}_{1.8}\text{O}_4$ spinel compared to distorted non-cubic Mn_3O_4 requires further discussion.

Coexistence of Fe^{2+} and Fe^{3+} at octahedral sites of MgFe_2O_4 spinel generates the $\text{Fe}^{2+}/\text{Fe}^{3+}$ hopping pair exhibiting n-type behavior with electrons as the main charge carrier. Both Mn^{4+} and Mn^{3+} at octahedral sites of Mn_3O_4 spinel generates an $\text{Mn}^{4+}/\text{Mn}^{3+}$ hopping pair, exhibiting p-type behavior with holes as the main charge carriers. As shown in Fig. 6, doping Mn cation in MgFe_2O_4 has a significant negative impact on electron hopping energy barrier and electrical conductivity. Also as explained in the discussion of Fig. 3, the nearest neighbor hopping is the most suitable model for the doped composite. The high polaron hopping energy barrier and poor conductivity of $\text{MgMn}_{0.2}\text{Fe}_{1.8}\text{O}_4$ are not due to structural distortion and low hopping probability since no significant deviation from a cubic structure was observed according to our XRD. Therefore, we associate the high energy barrier to the non-similar donor/acceptor pair elements of Fe and Mn, as illustrated in Fig. 8 (gray arrow). As a result, Mn doping in MgFe_2O_4 increases the energy barrier due to pairs of different elements without affecting nearest neighbor hopping as the dominant electron transport model. This is depicted in Fig. 8, where there is a relatively lower activation energy (black arrows) for same-element hopping, whereas a much higher activation energy (gray arrow) is required for hopping across different elements. This is similar to the cross-hopping phenomena previously described by Bhargava et al. [41].

4. Conclusion

Electron transport through cubic MgFe_2O_4 via the nearest neighbor hopping site at 423–523 K deviates toward variable range hopping of 0.62–0.72 eV through structurally distorted Mn_3O_4 . Such a high temperature variable range electron hopping has not been reported in the case of Mn_3O_4 . Replacing 10 mol% of Fe with Mn does not generate structural distortion, keeping the electron hopping model in the form of temperature independent activation energy the same as MgFe_2O_4 . The energy barrier of electron hopping through $\text{MgMn}_{0.2}\text{Fe}_{1.8}\text{O}_4$ stays higher than MgFe_2O_4 spinel, which is a consequence of non-similar donor/acceptor pairs of Fe/Mn. The electron barrier of Fe/Mn pair is higher than both $\text{Fe}^{2+}/\text{Fe}^{3+}$ donor/acceptor pairs. Because metal oxide spinels have numerous roles in sensors, catalysts, and energy and electronic applications, the fundamental insight into the mechanisms of conductivity shown here may assist those in the development of future technologies to develop better materials based on such understanding.

Funding

This research was funded by Natural Sciences and Engineering Research Council of Canada to Khashayar Ghandi.

Data availability statement

Sharing research data helps other researchers evaluate our findings, build on our work and to increase trust in our article. Therefore, the data will be shared by the corresponding author upon request.

Statements and declarations

The authors have no competing and commercial interests to declare that are relevant to the content of this article.

Prime novelty statement

1. The mechanism of electron hopping in bare Mn_3O_4 has not been reported yet, which is the most significant novelty of this work.
2. The energy barrier of Mn doped MgFe_2O_4 is higher than both bare MgFe_2O_4 and bare Mn_3O_4 which is reported here for the first time.

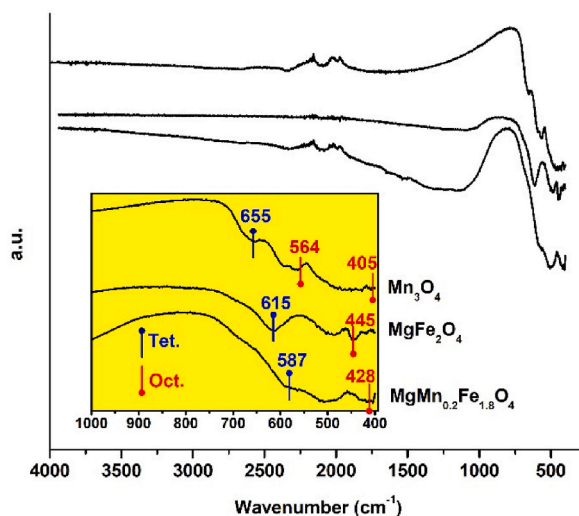


Fig. 7. FT-IR spectra of Mn_3O_4 , MgFe_2O_4 , and Mn-doped MgFe_2O_4 ($\text{MgMn}_{0.2}\text{Fe}_{1.8}\text{O}_4$).

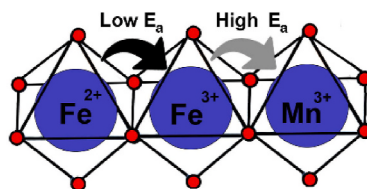


Fig. 8. The effect of coexistence of two different $\text{Fe}^{2+}/\text{Fe}^{3+}$ and $\text{Mn}^{4+}/\text{Mn}^{3+}$ hopping pairs.

CRediT authorship contribution statement

F. Farshidfar: Conceptualization, Data curation, Formal analysis, Investigation, Methodology, Visualization, Writing – original draft. **M. Lapolla:** Data curation, Visualization, Writing – review & editing. **A. Fattahi:** Data curation, Writing – review & editing. **K. Ghandi:** Conceptualization, Formal analysis, Funding acquisition, Investigation, Methodology, Project administration, Resources, Supervision, Validation, Writing – review & editing.

Declaration of competing interest

The authors declare that they have no known competing financial interests or personal relationships that could have appeared to influence the work reported in this paper.

Acknowledgments

This research was funded by Natural Sciences and Engineering Research Council of Canada to Khashayar Ghandi.

The authors would like to express their heartfelt dedication to all individuals in Iran who have been affected by human rights violations, including university students who have been harmed, faced unjust repercussions, or other forms of violence, for their pursuit of human rights and freedom. We stand with all those who continue to advocate for a more just and equitable future in Iran and around the world.

References

- [1] M. Singh, S.R. Bhardiya, A. Asati, H. Sheshma, A. Rai, V.K. Rai, Design of a sensitive electrochemical sensor based on ferrocene-reduced graphene oxide/Mn-spinel for hydrazine detection, *Electroanalysis* 33 (2021) 464–472.
- [2] T. Zhou, X. Liu, R. Zhang, L. Wang, T. Zhang, Constructing hierarchical heterostructured $\text{Mn}_3\text{O}_4/\text{Zn}_2\text{SnO}_4$ materials for efficient gas sensing reaction, *Adv. Mater. Interfac.* 5 (2018), 1800115.
- [3] W. Li, H. Cheng, L. Zhang, X. Wang, K. Qian, B. Zhang, J. Ma, X. He, Eg Orbital Occupancy-Dependent Intrinsic Catalytic Activity of Zn-Co-Mn Spinel Oxides for Peroxymonosulfate Activation, Available at: SSRN 4135622.
- [4] S. Wang, C. Chen, Y. Li, Q. Zhang, Y. Li, H. Gao, Synergistic effects of optical and photoluminescence properties, charge transfer, and photocatalytic activity in MgAl_2O_4 : Ce and Mn-codoped MgAl_2O_4 : Ce phosphors, *J. Electron. Mater.* 48 (2019) 6675–6685.

- [5] C. Li, X. Han, F. Cheng, Y. Hu, C. Chen, J. Chen, Phase and composition controllable synthesis of cobalt manganese spinel nanoparticles towards efficient oxygen electrocatalysis, *Nat. Commun.* 6 (2015) 7345.
- [6] F. Farshidfar, A. Fattahi, R. Brüning, D.H. Ryan, K. Ghandi, A creative method to tune Fe–O interaction in ferrites, *Journal of Advanced Ceramics* 12 (2023) 1612–1624.
- [7] E. Verwey, P. Haayman, F. Romeijn, Physical properties and cation arrangement of oxides with spinel structures II. Electronic conductivity, *J. Chem. Phys.* 15 (1947) 181–187.
- [8] K.E. Sickafus, J.M. Wills, N.W. Grimes, Structure of spinel, *J. Am. Ceram. Soc.* 82 (1999) 3279–3292.
- [9] M.P. Dojcinovic, Z.Z. Vasiljevic, V.P. Pavlovic, D. Barisic, D. Pajic, N.B. Tadic, M.V. Nikolic, Mixed Mg–Co spinel ferrites: structure, morphology, magnetic and photocatalytic properties, *J. Alloys Compd.* 855 (2021), 157429.
- [10] H.S.C. O'Neill, A. Navrotsky, Simple spinels; crystallographic parameters, cation radii, lattice energies, and cation distribution, *Am. Mineral.* 68 (1983) 181–194.
- [11] N. Aliyan, S.M. Mirkazemi, S.M. Masoudpanah, S. Akbari, The effect of post-calcination on cation distributions and magnetic properties of the coprecipitated MgFe₂O₄ nanoparticles, *Appl. Phys. A* 123 (2017) 446.
- [12] F. Driessens, Place and valence of the cations in Mn₃O₄ and some related manganates, *Inorg. Chim. Acta.* 1 (1967) 193–201.
- [13] S. Dorris, T.O. Mason, Electrical properties and cation valencies in Mn₃O₄, *J. Am. Ceram. Soc.* 71 (1988) 379–385.
- [14] F. Bosi, C. Biagioni, M. Passero, Nomenclature and classification of the spinel supergroup, *Eur. J. Mineral.* 31 (2018).
- [15] J. Cuenca, K. Bugler, S. Taylor, D. Morgan, P. Williams, J. Bauer, A. Porch, Study of the magnetite to maghemite transition using microwave permittivity and permeability measurements, *J. Phys. Condens. Matter: an Institute of Physics journal* 28 (2016), 106002.
- [16] R. Sharma, P. Thakur, P. Sharma, V. Sharma, Ferrimagnetic Ni²⁺-doped Mg-Zn spinel ferrite nanoparticles for high density information storage, *J. Alloys Compd.* 704 (2017) 7–17.
- [17] S. Riaz, A. Akbar, S. Naseem, Ferromagnetic effects in Cr-doped Fe₂O₃ thin films, *IEEE Trans. Magn.* 50 (2014) 1–4.
- [18] F. Farshidfar, A. Fattahi, R. Brüning, D.H. Ryan, K. Ghandi, A creative method to tune Fe–O interaction in ferrites, *Journal of Advanced Ceramics* (2023).
- [19] J. Guo, L. Shi, L. Wu, S. Pan, X. Yuan, J. Zhao, Spin-polarized electron transport in highly reduced MgFe₂O_{4-δ}, *Mater. Res. Express* 5 (2018), 126301.
- [20] M. Gateshki, V. Petkov, S.K. Pradhan, T. Vogt, Structure of nanocrystalline MgFe₂O₄ from X-ray diffraction, Rietveld and atomic pair distribution function analysis, *J. Appl. Crystallogr.* 38 (2005) 772–779.
- [21] R. Kambale, N. Adhate, B. Chougule, Y. Kolekar, Magnetic and dielectric properties of mixed spinel Ni–Zn ferrites synthesized by citrate–nitrate combustion method, *J. Alloys Compd.* 491 (2010) 372–377.
- [22] F. Farshidfar, A. Fattahi, R. Brüning, K. Ghandi, A Creative Method to Tune Fe-O Interaction in Ferrites *Advanced Ceramics*, 2023.
- [23] X. Li, Y. Xu, C. Wang, Suppression of Jahn–Teller distortion of spinel LiMn₂O₄ cathode, *J. Alloys Compd.* 479 (2009) 310–313.
- [24] D. Jarosch, Crystal structure refinement and reflectance measurements of hausmannite, Mn₃O₄, *Mineral. Petrol.* 37 (1987) 15–23.
- [25] B. Panalytical, P.P. Diffraktometer, Almelo, 2014. The Netherlands.
- [26] B. Panalytical, X'Pert HighScore Plus V4. 1, Almelo, The Netherlands, 2014.
- [27] T.A. Para, S.K. Sarkar, Challenges in rietveld refinement and structure visualization in ceramics, *Adv. Ceram. Mater.* (2021).
- [28] B.H. Toby, R factors in Rietveld analysis: how good is good enough? *Powder Diffr.* 21 (2006) 67–70.
- [29] M. Rudra, H. Tripathi, A. Dutta, T. Sinha, Existence of nearest-neighbor and variable range hopping in Pr₂ZnMnO₆ oxygen-intercalated pseudocapacitor electrode, *Mater. Chem. Phys.* 258 (2021), 123907.
- [30] E. Bertaut, Sur quelques progrès récents dans la cristallographie des spinelles, en particulier des ferrites, *J. Phys. Radium* 12 (1951) 252–255.
- [31] D.S. McClure, The distribution of transition metal cations in spinels, *J. Phys. Chem. Solid.* 3 (1957) 311–317.
- [32] R.A. Sutar, L. Kumari, M.V. M, Three-dimensional variable range hopping and thermally activated conduction mechanism of polypyrrole/zinc cobalt oxide nanocomposites, *J. Phys. Chem. C* 124 (2020) 21772–21781.
- [33] D.A. Landínez Téllez, D. Martínez Buitrago, R. Cardona C, E.W. Barrera, J. Roa-Rojas, Crystalline structure, magnetic response and electronic properties of RE₂MgTiO₆ (RE=Dy, Gd) double perovskites, *J. Mol. Struct.* 1067 (2014) 205–209.
- [34] S. Messerschmidt, A. Krampf, L. Vittadello, M. Imlau, T. Nörenberg, L.M. Eng, D. Emin, Small-polaron hopping and low-temperature (45–225 K) photo-induced transient absorption in magnesium-doped lithium niobate, *Crystals* 10 (2020) 809.
- [35] M. Naeem, N.A. Shah, I.H. Gul, A. Maqsood, Structural, electrical and magnetic characterization of Ni–Mg spinel ferrites, *J. Alloys Compd.* 487 (2009) 739–743.
- [36] H. Dhaouadi, A. Madani, F. Touati, Synthesis and spectroscopic investigations of Mn₃O₄ nanoparticles, *Mater. Lett.* 64 (2010) 2395–2398.
- [37] H. Dhaouadi, O. Ghodbane, F. Hosni, F. Touati, Mn₃O₄ Nanoparticles: Nanoparticles: Synthesis, Characterization, and Dielectric Properties, vol. 2012, ISRN Spectroscopy, 2012, 706398.
- [38] E.G. Larson, R.J. Arnott, D.G. Wickham, Preparation, semiconduction and low-temperature magnetization of the system Ni_{1-x}Mn_{12-x}O₄, *J. Phys. Chem. Solid.* 23 (1962) 1771–1781.
- [39] M. Rudra, S. Halder, S. Saha, A. Dutta, T. Sinha, Crossover between Variable Range Hopping and Small Polaron Hopping Mechanisms in Pr₂NiTiO₆ Double Perovskite Oxide..
- [40] M. Rudra, S. Halder, S. Saha, A. Dutta, T. Sinha, Temperature dependent conductivity mechanisms observed in Pr₂NiTiO₆, *Mater. Chem. Phys.* 230 (2019) 277–286.
- [41] A. Bhargava, R. Eppstein, J. Sun, M.A. Smeaton, H. Paik, L.F. Kourkoutis, D.G. Schlom, M. Caspary Toroker, R.D. Robinson, Breakdown of the small-polaron hopping model in higher-order spinels, *Adv. Mater.* 32 (2020), 2004490.
- [42] M. Ishii, M. Nakahira, T. Yamanaka, Infrared absorption spectra and cation distributions in (Mn, Fe)₃O₄, *Solid State Commun.* 11 (1972) 209–212.
- [43] S.B. Somvanshi, S.R. Patade, D.D. Andhare, S.A. Jadhav, M.V. Khedkar, P.B. Kharat, P.P. Khirade, K. Jadhav, Hyperthermic evaluation of oleic acid coated nano-spinel magnesium ferrite: enhancement via hydrophobic-to-hydrophilic surface transformation, *J. Alloys Compd.* 835 (2020), 155422.